Journal of Hazardous Materials 197 (2011) 119–127

Contents lists available at SciVerse ScienceDirect

Journal of Hazardous Materials

journal homepage: www.elsevier.com/locate/jhazmat

Trace contaminant concentration affects mineral transformation and pollutant fate in hydroxide-weathered Hanford sediments

Nicolas Perdrial[a,*], Nelson Rivera[b], Aaron Thompson[c], Peggy A. O'Day[b], Jon Chorover[a]

[a] Department of Soil, Water and Environmental Science, University of Arizona, 1177 E. Fourth St., Tucson, AZ 85721, USA
[b] School of Natural Sciences, University of California, Merced, CA 95343, USA
[c] Department of Crop and Soil Science, University of Georgia, Athens, GA 30602, USA

ARTICLE INFO

Article history:
Received 18 April 2011
Received in revised form 18 August 2011
Accepted 16 September 2011
Available online 22 September 2011

Keywords:
Zeolite
Feldspathoids
Strätlingite
Cesium
Strontium

ABSTRACT

Prior work has shown that when siliceous sediments are infused with caustic radioactive waste, contaminant fate is tightly coupled to ensuing mineral weathering reactions. However, the effects of local aqueous geochemical conditions on these reactions are poorly studied. Thus, we varied contaminant concentration and pCO_2 during the weathering of previously uncontaminated Hanford sediments over 6 months and 1 year in a solution of caustic waste (pH 13, high ionic strength). Co-contaminants Sr, Cs and I were added at "low" (Cs/Sr: 10^{-5} m; I: 10^{-7} m) and "high" (Cs/Sr: 10^{-3} m; I: 10^{-5} m) concentrations, and headspace was held at atmospheric or undetectable (<10 ppmv) CO_2 partial pressure. Solid phase characterization revealed the formation of the zeolite chabazite in "high" samples, whereas feldspathoids, sodalite and cancrinite, were formed preferentially in "low" samples. Sr, Cs and I were sequestered in all reacted sediments. Native calcite dissolution in the CO_2-free treatment drove the formation of strätlingite ($Ca_2Al_2SiO_7{\cdot}8H_2O$) and diminished availability of Si and Al for feldspathoid formation. Results indicate that pCO_2 and contaminant concentrations strongly affect contaminant speciation in waste-weathered sediments, and are therefore likely to impact reaction product stability under any remediation scenario.

1. Introduction

During the Cold War, the U.S. Department of Energy Hanford Site (WA) was the primary locale for plutonium extraction. For 40 years, large volumes of high-level radioactive waste (HLRW) were generated and stored in 177 buried single- and double-shell underground tanks [1,2]. Different chemical extraction and separation processes produced twenty-six chemically dissimilar waste streams that resulted in mixed tank wastes with elevated values of pH (8 to 14), ionic strength (2–16 M $NaNO_3$), temperature (60–110 °C), and dissolved aluminum [3–6]. Sixty-eight out of 149 single-shell tanks are suspected to have leaked, releasing millions of liters of HLRW waste to the vadose zone. According to Zachara et al. [7], vadose zone sediments are contaminated with various radionuclides, with ^{90}Sr, ^{137}Cs and ^{129}I among the most abundant (10^{-4} to 10^{-1} Ci L^{-1} for Sr, 5×10^{-2} to 8×10^{-1} Ci L^{-1} for Cs and 1 to 5×10^{-12} Ci L^{-1} for I [8]). Transport of contaminants from tank leaks to the Columbia River poses an important health risk to humans [9], emphasizing the need to characterize mechanisms of contaminant retardation in the vadose zone. To predict waste plume migration and understand possible mechanisms of radionuclide sequestration at the Hanford Site, the impact of caustic waste leachate on surrounding sediments and transport processes must be elucidated.

Previous laboratory experiments on monomineralic systems showed that synthetic tank waste leachate (STWL) solutions dissolve primary tectosilicates [10–12], and clay minerals [13–15], resulting in silicon release. Silicon release into hyperalkaline, Al-rich STWL solution results in aqueous phase supersaturation with respect to highly reactive feldspathoid and zeolite minerals that precipitate from solution [10,11,14,16–20]. Reaction of multi-component Hanford sediments with STWL likewise revealed primary mineral dissolution and precipitation of feldspathoids NO_3-cancrinite and NO_3-sodalite [19–21], and zeolite A [19].

Kinetic studies showed a time dependency of primary phase dissolution, neophase formation, and contaminant sorption. Qafoku et al. [21] suggested that NO_3-sodalite forms early, transforming to NO_3-cancrinite by dissolution–reprecipitation. Both neophases are capable of co-precipitating significant amounts of cationic Cs and Sr into framework and cage sites [10,11,14,16,17], whereas uptake of iodide by such cation exchangers is likely limited. When STWL solutions are spiked with Si in the presence of cations (Cs, K, Sr, Ca, Mg, Al, Na), both sodalite and cancrinite precipitate and a ~1:1 Si:Al molar ratio zeolite forms at either high Cs concentration (500 mM)

* Corresponding author. Tel.: +1 520 626 1566; fax: +1 520 621 1647.
E-mail address: perdrial@email.arizona.edu (N. Perdrial).

0304-3894/$ – see front matter © 2011 Elsevier B.V. All rights reserved.
doi:10.1016/j.jhazmat.2011.09.063

[22] or short reaction time [23]. Furthermore, the presence of K^+ and divalent cations (Mg, Ca, Sr) slows the precipitation of cancrinite and sodalite in STWL solutions [22].

Prior studies of contaminant uptake by Hanford sediment, showed that Cs^+ sorbs selectively on frayed-edges and interlamellae of native micaceous minerals (illite, biotite, muscovite, and vermiculite) [5,6,24,25]. Conversely, a large fraction of Sr^{2+} sorbed to labile ion exchange sites (Mg^{2+} exchangeable) early in the sediment-STWL reaction sequence becomes increasingly recalcitrant to Mg^{2+} exchange over months to years of reaction time, and EXAFS data indicate Sr incorporation into zeolite and feldspathoid neophases [11]. Uncontaminated Hanford sediments were previously reacted for 6 months with STWL containing low concentration of Cs and Sr (10^{-5} m) and I (10^{-7} m), and contaminant release was investigated in column experiments designed to model the removal of the caustic source wherein a synthetic background pore water was infiltrated through STWL-reacted sediments [25]. Transport simulation showed that Cs release depends on ion exchange even at long desorption times, whereas Sr release was consistent with dissolution from feldspathoid at steady-state. Additionally, contaminant desorption from sediments reacted in CO_2-free environments was higher than desorption from sediments reacted at atmospheric pCO_2 [25]. Iodide behavior is controlled by ion exchange on protonated mineral surface hydroxyl groups [26,27], leading to high mobility and limited retention in the sediments, particularly at high pH. No desorption study has been carried out on iodide in STWL-reacted in Hanford sediments.

In monomineralic systems, initial Cs and Sr concentrations strongly affect the rate of tetrahedral Al (Al^{IV}) solid phase formation, with more rapid precipitation at lower Cs/Sr concentration. Our prior studies [13,14,16] indicated that despite high (2 M) background Na^+ concentration in STWL, the rate of incongruent weathering of specimen clay minerals exhibited negative dependence on trace contaminant concentration (10^{-5} to 10^{-3} m). Also, at high contaminant concentration, Cs and Sr partitions into less crystalline solids that dissolve readily upon a shift to fresh water leaching [13,14,16], whereas at lower concentrations, they are bound into more dissolution-recalcitrant species [17]. In so far as they affect mineral transformation rates, Sr and Cs concentrations may therefore control the rate of their own sequestration into recalcitrant solid-phase weathering products. In specimen mineral systems, (i) the concentrations of contaminants [14] and (ii) the presence of free cations [22] combine with reactant mineralogy [11,13,16] to control the couplings between mineral weathering and contaminant fate. We postulate similar processes affect contaminant uptake in complex Hanford sediments.

Although present at trace concentration relative to background Na^+, the prevalence of Sr^{2+} and Cs^+ nonetheless affects mineral transformation rates measured in specimen clay systems. The extent to which the same effect occurs in complex natural sediments thus remains unclear [11] and warrants high-resolution geochemical research. In the current study, we tested this effect using detailed synchrotron-based X-ray diffraction and spectroscopy to characterize Hanford sediment weathering induced by STWL reaction. Two contaminant concentrations and two different pCO_2 levels (presence and absence of atmospheric CO_2) were used to span the ranges of those parameters expected in the field. Variations in pCO_2 should affect the stability of carbonate species. Since prior work indicates that contaminant release is controlled by mineral dissolution [25], a precise characterization and quantification of reaction products is needed to predict the fate of STWL-weathering products upon re-introduction of native porewater solutions. This study aims to facilitate predictive modeling of contaminant fate at Hanford by providing an improved understanding of waste-sediment reactions.

2. Material and methods

2.1. Sample collection

Sediments similar in character to those beneath the leaking tanks at the DOE Hanford Site were collected from the 218-E-12B Burial Ground excavation site [28], an uncontaminated area within the Hanford Formation. Sediments were air dried, sieved to obtain the <2 mm fraction, and used without further modification. This material is referred to as Hanford sediment (HS) in the following text.

2.2. Reaction procedure

We modified and upscaled the experimental conditions used by Chorover and co-workers [11,13,16,17] to simulate the contamination of pristine HS with Sr, Cs and I present in hyperalkaline solutions (see S-1 of the supplementary material for details). Briefly, 400 g of air-dry sediment were reacted with 20 kg of STWL. CsCl, $SrCl_2{\cdot}6H_2O$ and NaI were added to the STWL stock solution as "co-contaminants" to give treatments with two initial aqueous-phase concentrations termed "HIGH" (10^{-3} m Cs^+ and Sr^{2+} and 10^{-5} m I^-) and "LOW" (10^{-5} m Cs^+ and Sr^{2+} and 10^{-7} m I^-).

Sediments were reacted with STWL in carboys for 6 or 12 mo (182 or 365 d) in a 2×2 experimental matrix of four different aqueous geochemical conditions: STWL with LOW and HIGH contaminant concentrations reacted in atmospheric pCO_2 ($[+CO_2]$) and CO_2-free ($[-CO_2]$) environments. This yielded eight sets of reaction products.

2.3. Solid phase characterization

Total element concentrations were measured by ICP-MS following Li-metaborate fusion [29] and INAA for iodine. For particle size analysis, water-suspended samples, sonicated for 10 s were analyzed with a Beckman Coulter LS 13 320 Laser Diffraction Particle Size Analyzer (Fullerton, CA). Cation exchange capacities (CEC) were determined by exchanging cations with cobalt-hexamine-chloride (Cohex–$[Co(NH_3)_6]Cl_3$) [30]. In this case, 2 g of sediment were mixed with 25 mL of 12 mmol L^{-1} Cohex and shaken for 2 h (corresponding to maximum exchange). CEC values were calculated from the loss of Co from solution (ICP-MS, PerkinElmer Elan DRC). External specific surface areas were determined using dinitrogen BET (Beckman Coulter SA-3100).

Diffuse reflectance Fourier transform infrared (DRIFT) spectra of the sediment samples were obtained on a Nicolet Magna 560 FTIR spectrometer (Thermo Sci., Waltham, MA) by averaging 400 scans per sample across the frequency range of 4000–400 cm^{-1} (optical resolution of 4 cm^{-1}). Sample preparation consisted of grinding 9 mg of freeze-dried sediment with 441 mg of ground analytical spectroscopy-grade KBr crystals. X-ray diffractograms, acquired on the bulk and isolated fine fraction (FF) of all samples (see S-2 of the supplementary material), were collected at the Stanford Synchrotron Radiation Lightsource (SSRL) on beam line 11-3 operating at ~12735 eV in transmission mode, using a 345 mm radius Mar detector with 100 μm pixels. Approximately 0.05 g of sample was packed between two layers of Scotch Magic tape to obtain a homogeneous thin layer sample. After calibration of the detector using finely ground LaB_6 crystals, five scans were combined per sample. Data were reduced using the Advanced Diffraction Machine software [31] with a mask covering the beamstop. Patterns were added, reduced, corrected from residual quartz saturation and systematic displacement and converted to those associated with Cu-Kα radiation wavelength. Quantitative phase analysis was performed using the Rietveld module included in the X'Pert HighScore Plus software, details of the procedure for analysis are given in Section S-3

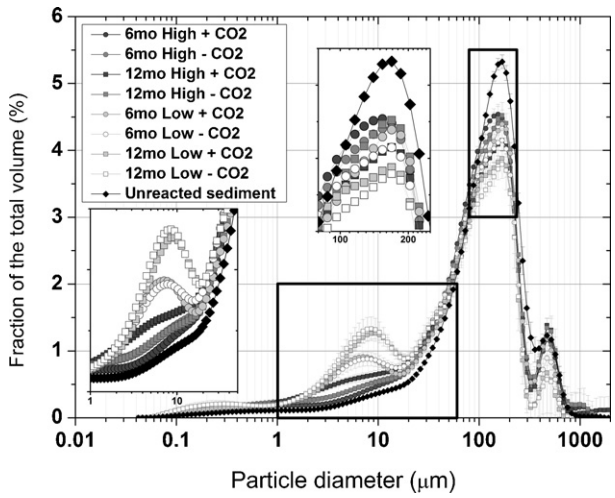

Fig. 1. Particle size distribution of batch-weathered sediments and unreacted material by laser granulometry in % of the volume.

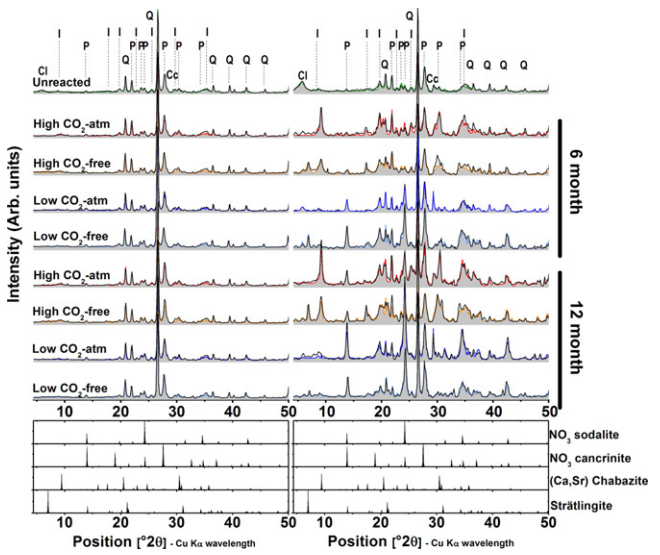

Fig. 2. X-ray diffractograms (black lines) and Rietveld simulated spectrum (colored lines and grey area) of the bulk sediments (left panel) and the fine fraction (FF) extracts (right panel). Bottom diffractograms represent simulated pattern of NO_3-sodalite based on data from [33], simulated pattern of a NO_3-cancrinite based on data from [34], simulated pattern of a Ca–Sr chabazite based on data from [35] and simulated pattern of a strätlingite based on data from [36]. Main reflections in the unreacted are labeled (upper diffractograms) with Q for quartz, P for plagioclase, I for illite, Cl for chlorite and Cc for calcite.

(supplementary material). For microscopy, 9 μL of dilute representative samples were pipetted onto copper transmission electron microscopy (TEM) grids and examined using a Hitachi H8100 LaB_6 TEM operating at 200 kV coupled with a Thermo NORAN energy-dispersive X-ray spectrometer (EDS).

Strontium K-edge X-ray absorption spectra of the FF were acquired at SSRL on beam lines 11-2 and 4-1 under dedicated conditions (3 GeV, 80–100 mA). Spectra were collected using a Si(2 2 0) monochromator crystal (vertical beam size = 1 mm) and a focused beam. A rhodium mirror was used for harmonic rejection (17 keV cutoff energy), allowing for a fully tuned beam. Beam energy was calibrated with a $SrCO_3$(s) standard with the energy at the midpoint of the edge jump set to 16105 eV. Sediment FF extracts were packed evenly in Teflon holders and sealed with Kapton tape. Samples were held in a He cryostat at 3–5 K during data collection. Fluorescence absorption spectra were collected using a solid-state Ge-array detector and successive scans (6–12) were averaged. Details of data analysis and reference materials are reported in Section S-4 (supplementary material).

3. Results

3.1. Sediment physical characteristics

Following reaction with STWL, the mass fractions of clay and silt increased at the expense of the sand fraction resulting in an overall decrease in sediment particle size (Table 1). Despite this, sediment CEC_{Cohex} and SSA_{ext} also decreased with reaction (Table 1). HIGH-reacted sediments generally exhibited lower CEC and SSA relative to LOW-reacted sediments. SSA increased slightly between 6 and 12 months of reaction, whereas CEC decreased. Particle size distribution (p.s.d., Fig. 1) showed an emergent post-reaction size mode between 1 and 10 μm whose proportional contribution to the p.s.d. increased with reaction time. Sediments reacted at LOW contained a higher proportion of fine-sized particles, which increased strongly between 6 and 12 mo of reaction. This new mode was accompanied by a relative increase in fine clay (0.06–0.60 μm) and a decrease in sand-sized particles.

3.2. Contaminant uptake by sediment

Compared to the unreacted material, reacted sediments show an increase in solid phase Sr, Cs, I, Na, K and Al concentration and a decrease in Ca (Table 2). For all treatments, Sr uptake is an order of magnitude higher than Cs uptake. No significant differences were observed for I uptake between HIGH and LOW. The 12-month LOW treatment exhibits the highest Na and Al uptake. Strontium and Cs contaminant uptake was not affected by pCO_2 in the LOW; however in the HIGH, Sr and Cs uptake was greater in the CO_2-free treatments (except at 12 mo for Sr). Strontium, Cs and I uptake showed no clear time dependency (Table 2).

3.3. Mineral transformations

Rietveld phase quantification of the bulk HS (Fig. 2 and Table S-5, supplementary material) indicates that the sediments are dominated by quartz, plagioclase and mica with smaller amounts of calcite and chlorite. Phase quantification for the HS FF (Fig. 2 and Table 3) shows an increase in the signal for phyllosilicates (illite, chlorite and kaolinite) relative to the bulk. Due to peak-overlap with 14 Å clay minerals, the reported chlorite abundance may include swelling clay minerals (vermiculite, smectite). As plagioclase and sodalite share very similar diffraction patterns it is likely that the apparent increase in plagioclase (Table S-4) in reacted sediments corresponds to an underestimation of sodalite. We can correct for this interference by assuming an equal abundance of plagioclase in the reacted HIGH and LOW treatments, assigning the difference to feldspathoid abundance. The range of feldspathoid mass fractions are then 5.6–8.6% in the 6 mo $LOW_{[+CO_2]}$, 2.6–3.6% in the 6 mo $LOW_{[-CO_2]}$, 3.1–10.4% in the 12 mo $LOW_{[+CO_2]}$ and 2.4–11.4% in the 12 mo $LOW_{[-CO_2]}$. Relative to unreacted HS, reacted samples contain (per unit mass) (i) less mica, (ii) more plagioclase, (iii) no calcite in the CO_2-free reacted samples, and iv) neoprecipitated phases whose composition is treatment dependent (Fig. 2, Table S-5). Across all treatments and reaction times, the neophases formed include a Sr–Ca rich chabazite $[(Ca,Sr)_2Al_4Si_8O_{24}{\cdot}13H_2O]$ in the HIGH, NO_3-sodalite $[Na_8(AlSiO_4)_6{\cdot}(NO_3)_2]$ and NO_3-cancrinite $[Na_8(AlSiO_4)_6(NO_3)_2{\cdot}2H_2O]$ in the LOW, and strätlingite $[Ca_2Al_2SiO_7{\cdot}8(H_2O)]$ in the $[-CO_2]$ treatments. Generally, the relative mass fractions of neophase precipitates are elevated in the HIGH (6–10%) relative

Table 1
Texture, specific surface area (SSA) and cationic exchange capacity (CEC) of the unreacted and the reacted Hanford sediment (standard deviations in underscript).

Sample name	Particle size distribution ($g\,kg^{-1}$)[a]			SSA_{ext}[b] $m^2\,g^{-1}$	CEC[c] $mmol_c\,kg^{-1}$
	Sand	Silt	Clay		
Hanford sediment[d]	$802.57_{1.83}$	$167.75_{1.54}$	$29.75_{0.37}$	$12.33_{0.05}$	$87.94_{2.52}$
6 mo HIGH$_{[+CO_2]}$	$736.70_{2.63}$	$217.40_{2.17}$	$45.93_{0.48}$	$8.88_{0.04}$	$58.17_{1.27}$
6 mo HIGH$_{[-CO_2]}$	$699.33_{1.20}$	$240.17_{0.81}$	$60.50_{0.46}$	$8.35_{0.04}$	$53.70_{2.48}$
6 mo LOW$_{[+CO_2]}$	$662.00_{10.82}$	$289.13_{9.10}$	$48.87_{1.73}$	$9.33_{0.06}$	$75.02_{0.04}$
6 mo LOW$_{[-CO_2]}$	$637.33_{15.30}$	$308.43_{11.41}$	$54.23_{3.90}$	$9.49_{0.09}$	$59.40_{1.40}$
12 mo HIGH$_{[+CO_2]}$	$670.70_{12.75}$	$271.80_{9.95}$	$57.57_{4.82}$	$8.90_{0.01}$	$56.19_{0.56}$
12 mo HIGH$_{[-CO_2]}$	$716.23_{9.74}$	$227.17_{7.08}$	$56.50_{2.06}$	$8.90_{0.06}$	$55.16_{2.66}$
12 mo LOW$_{[+CO_2]}$	$591.67_{15.43}$	$352.27_{13.08}$	$56.07_{2.37}$	$9.72_{0.09}$	$65.92_{0.03}$
12 mo LOW$_{[-CO_2]}$	$575.76_{24.81}$	$358.05_{18.88}$	$66.20_{5.93}$	$10.94_{0.12}$	$50.93_{1.49}$

[a] Particle size distribution measured by laser diffraction granulometry.
[b] Total specific surface area measured by N_2(g) adsorption.
[c] CEC measured using the Cohex exchange method.
[d] Values from Thompson et al. [24].

Table 2
Concentrations in Sr, Cs, I, Si, Al, Na, Ca and K in the sediments.

	Sr	Cs	I[a]	Si	Al	Na	Ca	K
	$mmol\,kg^{-1}$							
Unreacted Hanford sediment[b]	$4.34_{0.2}$[c]	$0.023_{0.002}$	bd[d]	$10{,}780_{108}$	2483_{50}	787.4	$724_{0.27}$	394.9
6 mo HIGH$_{[+CO_2]}$	$38.80_{2.8}$	$3.30_{0.07}$	0.022	$10{,}817_{156}$	$2653_{57\cdot9}$	$1097_{4.6}$	$659.8_{7.6}$	$397.0_{3.0}$
6 mo HIGH$_{[-CO_2]}$	$50.62_{0.8}$	$4.11_{0.25}$	0.043	$10{,}616_{126}$	$2716_{18\cdot0}$	$1015_{11.4}$	$650.0_{24.0}$	$403.4_{18.0}$
6 mo LOW$_{[+CO_2]}$ [b]	$4.60_{0.2}$	$0.100_{0.001}$	0.014	$10{,}770_{4.71}$	$2732_{16\cdot6}$	$1315_{16.0}$	$675.8_{2.6}$	$397.0_{0.00}$
6 mo LOW$_{[-CO_2]}$ [b]	$4.59_{0.2}$	$0.096_{0.007}$	0.035	$10{,}930_{109}$	$2734_{55.0}$	1197	$643.7_{24.0}$	399.2
12 mo HIGH$_{[+CO_2]}$	$46.76_{2.2}$	$3.24_{0.27}$	0.037	$10{,}334_{330}$	$2737_{65.2}$	$1333_{0.00}$	$648.2_{8.83}$	$392.8_{18.0}$
12 mo HIGH$_{[-CO_2]}$	47.00	3.80	0.040	10,757	2813	1120	659.8	409.8
12 mo LOW$_{[+CO_2]}$	$4.54_{0.46}$	$0.102_{0.003}$	0.039	$10{,}397_{300}$	$2860_{88.77}$	1538_{217}	$653.5_{3.78}$	$383.2_{13.5}$
12 mo LOW$_{[-CO_2]}$	5.19	0.126	0.035	10,809	2832	1368	661.6	390.7

Limits of detection ($mmol\,kg^{-1}$) Sr: 0.02, Cs: 0.0007, I: 0.004, Si: 1.66, Al: 1.88, Na: 2.6, Ca: 2.5 and K: 3.0.
[a] Analyzed by INAA.
[b] Values (except I) from Thompson et al. [24].
[c] Errors are the standard deviation.
[d] Below detection.

to LOW (2–6%) treatment. Outside of its previous identification in LOW waste-impacted sediments [25], strätlingite has only been reported to form at room temperature in hyperalkaline, aluminum-rich cements [32].

By isolating the FF, the signal-to-noise associated with fine precipitate particles was effectively increased. In the LOW 6 and 12 mo and HIGH 12 mo samples, reflections at 14°, 34.2° and 42.6° 2θ are consistent with those of NO_3-sodalite and NO_3-cancrinite. The 24.3° 2θ reflection is typical of sodalite, whereas the 19° 2θ is typical of cancrinite. For the HIGH, dominant neophase reflections at 9.1°, 20.8° and 30.3° 2θ are characteristic of Ca–Sr chabazite.

Neophase formation is impacted by CO_2 abundance. For the [+CO_2] sediments (both LOW and HIGH), the native calcite reflection (29.5° 2θ) is preserved, whereas it is not detectable in the [−CO_2] sediments. Conversely, new reflections at 7° and 21.4° 2θ, associated with strätlingite arise in the [−CO_2] sediments that do not occur in the [+CO_2] sediments and HS. Rietveld quantifications of all FF (Table 3) show that neophase precipitates (22.5–43.9 mass% of the FF) are formed in association with dissolution of quartz, albite and chlorite, augmented by calcite dissolution only in the [−CO_2] treatments. The amount of feldspathoids (sodalite and cancrinite) increases with reaction time in the LOW. In the HIGH, the amount of chabazite increases with time in the [−CO_2] treatment, whereas in the [+CO_2] treatment, chabazite decreases in mass fraction as feldspathoids appear after 12 mo of reaction.

Diffuse reflectance infrared Fourier transform (DRIFT) spectra of the sediments (Fig. 3) show that absorption bands (at 1380 and 1420 cm^{-1}) characteristic of nitrate-containing secondary solids [11] appear after 6 mo and increase in intensity after 12 mo of reaction (Fig. 3b) in LOW treatments. The same bands are undetectable in the HIGH treatments after 6 mo and only slightly visible after 12 mo of reaction. The presence of the sharp band at 1380 cm^{-1} indicates the enclathration of NO_3 within sodalite cages, whereas a split from 1380 to 1410 cm^{-1} corresponds to the arrangement of nitrate anions in the cancrinite hexagonal channels [34]. For the HIGH treatments, NO_3-feldspathoids are detected only after 12 mo reaction, when low intensity bands appear at 1379 cm^{-1} and ~1420 cm^{-1} in the HIGH spectra (Fig. 3b). Thus, consistent with the

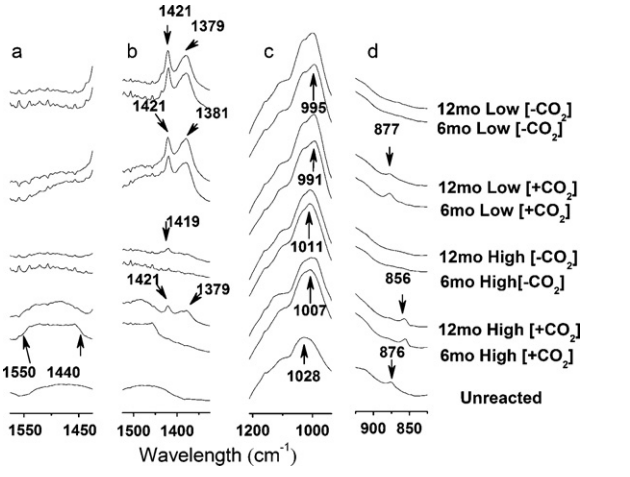

Fig. 3. FTIR spectra of the unreacted and the reacted sediments. The various regions are plotted separately to allow an expansion of the Y scale between (a) 1425 and 1580 cm^{-1}, (b) 1325 and 1525 cm^{-1}, (c) 950 and 1225 cm^{-1} and (d) 825 and 925 cm^{-1}.

Table 3
Quantitative results (in %) of the Rietveld simulation performed on the unreacted and reacted fine fraction extracts.

Sample name	Quartz SiO_2	Albite $NaAlSi_3O_8$	Andesine $(Ca,Na)(Al,Si)_4O_8$	Illite $K(Al,Mg,Fe)_2(Si,Al)_4O_{10}[(OH)_2\cdot(H_2O)]$	Chlorite $(Fe,Mg,Al)_6(Si,Al)_4O_{10}(OH)_8$	Kaolinite $Al_2Si_2O_5(OH)_4$	Calcite $CaCO_3$	Sr,Ca chabazite $Ca_{1.4}Sr_{0.3}Al_{3.8}Si_{8.3}O_{24}\cdot 13H_2O$	NO_3-sodalite $Na_8(AlSiO_4)_6(NO_3)_2$	NO_3-cancrinite $Na_{7.6}(AlSiO_4)_6(NO_3)_{1.6}(H_2O)_2$	Strätlingite $Ca_2Al_2SiO_7\cdot 8(H_2O)$	χ^2 [a]
Hanford	26.8	11.6	18.1	24.6	14.8	1.0	3.1	0.0	0.0	0.0	0.0	3.8
6 mo High $+CO_2$	15.8	11.9	7.9	47.2	0.0	1.5	1.4	14.2	0.0	0.0	0.0	11.8
6 mo High $-CO_2$	14.3	6.8	14.8	28.1	0.5	0.0	0.0	20.0	0.0	0.0	15.5	13.3
6 mo Low $+CO_2$	24.8	4.0	18.7	20.2	8.0	2.3	7.3	0.2	10.6	4.0	0.0	15.4
6 mo Low $-CO_2$	20.5	10.6	6.6	22.1	3.7	2.1	0.0	4.0	11.1	11.2	8.3	8.7
12 mo High $+CO_2$	14.5	5.5	12.5	37.8	1.1	0.0	2.2	13.9	8.8	3.7	0.00	12.4
12 mo High $-CO_2$	13.4	6.2	5.6	30.0	0.9	1.0	0.0	27.9	0.2	0.4	14.4	5.1
12 mo Low $+CO_2$	17.7	5.9	6.2	27.5	1.1	2.1	6.4	0.1	23.6	9.3	0.0	8.3
12 mo Low $-CO_2$	20.2	6.6	4.6	17.1	1.6	0.7	0.0	1.3	29.0	16.1	2.8	7.4

[a] χ^2 represents the goodness of fit and correspond to $\chi^2 = [\sum_i (I_{obs} - I_{calc})i^2/\sigma^2(I_{obs})i]/(n-p)$; with I the intensity, $\sigma(I_{obs})$ the estimated error of the measure (fixed to 10% of the counts), n the number of points used for simulation and p the number of parameters estimated.

XRD results, FTIR data indicate NO_3-feldspathoids appear later in sediment reacted with high contaminant concentrations.

The shifting of the Si–O–Si(Al) stretching band to lower frequencies (Fig. 3c – from 1028 to ~1011 cm^{-1} for the HIGH and to ~995 cm^{-1} for the LOW) indicates that the molar Si/Al ratio of tectosilicates decreases upon reaction (relative to primary minerals in the unreacted sediment [11]) and that neoprecipitates in the LOW samples have a Si/Al ratio lower than that of the HIGH. The relatively broad bands between 1440 and 1550 cm^{-1} (Fig. 3a) and a sharp band of low intensity around 870 cm^{-1} (Fig. 3d) that only exist in the unreacted sediments and in the [$+CO_2$] treatments are attributed to asymmetric stretching (1425 and 1550 cm^{-1} bands) and out-of-plane bending (870 cm^{-1} band) of the CO_3^{2-} anion in calcite ([37,38]). However, the low intensity of the out-of-plane bending at 870 cm^{-1} and the presence of the 856 cm^{-1} band in the $HIGH_{[+CO_2]}$ can be attributed to structural CO_3 in cancrinite [39] or strontianite [40]. These results are consistent with the expected effect whereby removal of CO_2 from STWL reaction diminishes the relative saturation of solution with respect to carbonate minerals.

Secondary phases were observed in the reacted sediments using TEM/EDS. Neoprecipitates crystallizing in the HIGH consisted of spheroids (Fig. 4a–d), whereas in the LOW, intergrowths of disk-shaped crystals were observed (Fig. 4e–h). Corresponding EDS analysis revealed that despite different morphologies, precipitates had similar compositions dominated by Si and Al (molar ratio ~1) with significant amounts of Na and Ca, and consistent presence of Fe. In the HIGH, Sr and Cs were detected in the precipitates, along with K. Due to strong overlap between Ca Kα and I Lα emission lines, iodine cannot be detected by EDS (or XAS) in the studied material. Although we did not detect the contaminants in association with other mineral phase, we do not rule out non-detectable Cs adsorbed to phyllosilicates. Both the morphology and chemical composition of the neoprecipitates are consistent with the presence of a sodalite/cancrinite-type feldspathoid in the LOW and a Na–Ca zeolite in the HIGH, and the solid phase accumulation of Al, Na, Sr, and Cs (Table 2). Iodine accumulation in reacted solids is also evident (Table 2), although at much lower – EDS undetectable – levels.

3.4. Strontium EXAFS

Linear combination fits of EXAFS spectra of the FF showed that Sr is associated with different reaction products depending on pCO_2 and contaminant concentration (Fig. 5, Table 4). In $HIGH_{[+CO_2]}$ samples, a fraction of Sr was associated with a $SrCO_3$-like phase not detected by XRD. As discussed in prior studies, this phase tends to dominate the EXAFS spectrum if present, although it does not constitute a major Sr-bearing component [11,17]. It was not detected in LOW or [$-CO_2$] treatments. Strontium-bearing neophases in HIGH samples identified by EXAFS were either mixed sodalite/cancrinite, chabazite, or a mixture of the two (Table 4). The spectra of $HIGH_{[-CO_2]}$ samples (6 and 12 mo) could be well fit with only the chabazite reference compound (natural sample) in which Sr substitutes for Ca. The chabazite EXAFS spectrum has features characteristic of a slightly longer average first-shell Sr–O distance (2.67 Å) and stronger second neighbor Sr–Si/Al scattering compared to the other reference compounds (Fig. 5, Table S-6, supplementary material). The amplitude of the second-neighbor Si/Al peak at 3.45 Å is greater in the sediment spectra than in the chabazite reference compound. Individual shell fits (not shown) indicate ~25% increase in the second-neighbor scattering amplitude but no difference in Sr–Si/Al interatomic distance. Strontium substitution for Ca in chabazite is consistent with results from XRD, which also indicated the presence of strätlingite, another Ca-bearing neophase that may contain Sr, in $HIGH_{[-CO_2]}$ samples (Table 3). Theoretical fits of the EXAFS spectra using Sr substituted for Ca in the

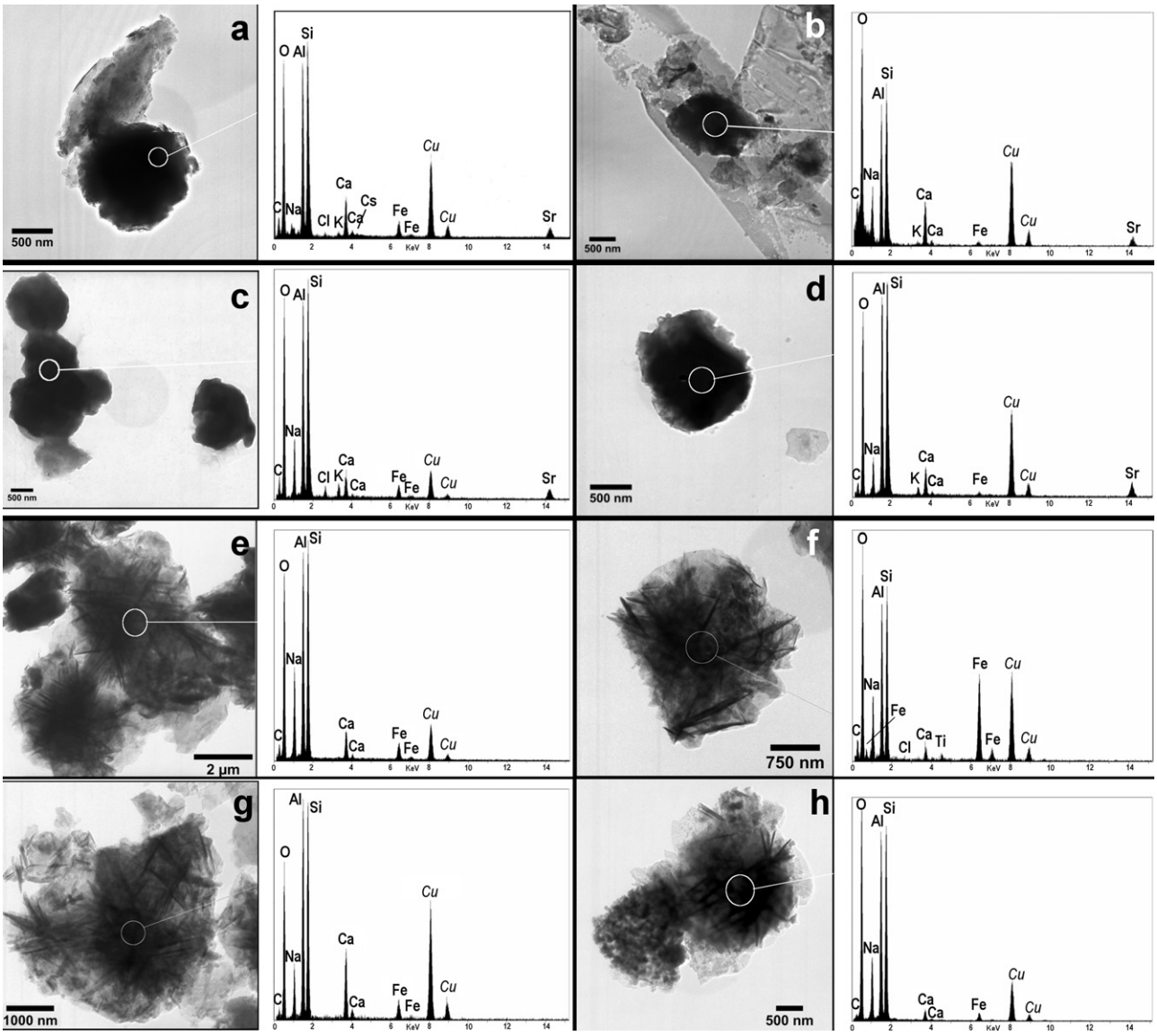

Fig. 4. TEM micrograph of spheroidal zeolite and corresponding EDS microanalysis in (a) 6mo HIGH[+CO_2], (b) 12 mo HIGH[+CO_2], (c) 6 mo HIGH[−CO_2], (d) 12 mo HIGH[−CO_2]. TEM micrograph of disk-shaped feldspathoids and corresponding EDS microanalysis in (e) 6 mo LOW[+CO_2], (f) 12 mo LOW[+CO_2], (g) 6 mo LOW[−CO_2], (h) 12 mo LOW[−CO_2]. For all EDS spectra, Cu peaks relate to the grid.

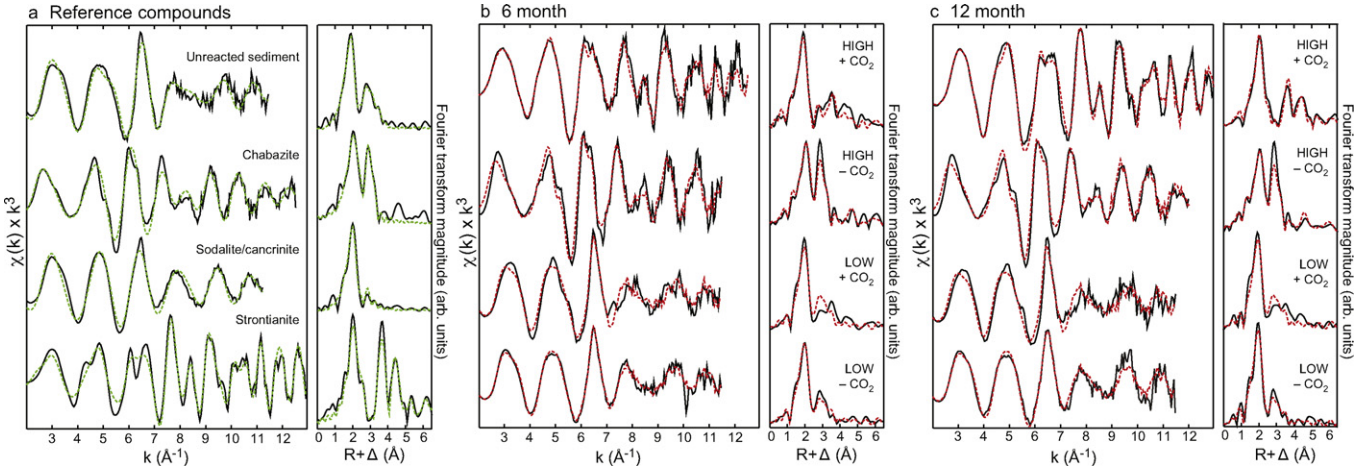

Fig. 5. Strontium K-edge EXAFS of (a) reference compounds, (b) 6 mo FF reacted sediments and (c) 12 mo FF reacted sediments. Dashed lines in (a) are non-linear least-squares fits of individual atomic shells using theoretical phase shift and amplitude functions (numerical results reported in Table S-5); in (b) and (c), dashed lines are linear combination least-squares fits using the reference compounds shown in a) (fit results are reported in Table 4).

Table 4
Linear combination fits (in percent of component) of EXAFS spectra for reacted sediments (FF).

Sample	Unreacted sediment[a]	Strontianite ($SrCO_3$)[a]	Sodalite/cancrinite[a]	Chabazite[a]	Total
6 mo High [+CO_2]	0	29 ± 2	32 ± 4	42 ± 4	103 ± 6
6 mo High [−CO_2]	0	0	0	114 ± 4	114 ± 4
6 mo Low [+CO_2]	94 ± 5	0	13 ± 4	0	107 ± 7
6 mo Low [−CO_2]	67 ± 4	0	31 ± 3	0	98 ± 4
12 mo High [+CO_2]	0	49 ± 1	49 ± 2	0	98 ± 3
12 mo High [−CO_2]	0	0	0	112 ± 3	112 ± 3
12 mo Low [+CO_2]	85 ± 6	0	20 ± 4	0	105 ± 7
12 mo Low [−CO_2]	50 ± 6	0	48 ± 5	0	98 ± 8

[a] See Table S-6 (supporting information) for EXAFS analysis of reference compounds. Error in component percent is from the statistical estimated standard deviation of the fit.

strätlingite structure suggested overlap and cancellation of second-neighbor Al and Ca atoms with Si/Al backscattering in chabazite, all at similar interatomic distances (no experimental reference spectra for strätlingite were available). Therefore, incorporation of Sr into strätlingite could not be determined from EXAFS analysis.

Linear combination fits of LOW FF samples indicated a large fraction of unreacted sediment (~50–94%) in addition to a sodalite/cancrinite phase whose contribution to the fits increased with aging time between 6 and 12 mo. It is likely that a portion of the component fit as unreacted sediment is actually a feldspathoid neophase. Strontium in the unreacted sediment was assumed to partially substitute for Ca in plagioclases (Table S-6). In Sr-bearing plagioclases, interatomic distances of Sr–Si/Al backscattering atoms range between ~3.3 and 4.0 Å [41]. The unreacted sediment spectrum was fit with a simplified model of two Si/Al shells (at 3.34 and 3.80 Å) and a Ca shell (at 4.13 Å) (in addition to first-shell O). Cation sites in feldspathoids have interatomic distances to framework Si/Al within the range of Si/Al backscattering in plagioclases. For linear combination fits of the FF spectra, the feldspathoid reference spectrum was a synthetic precipitate of Sr-bearing aluminosilicate identified as a mixed sodalite/cancrinite [23]. For $LOW_{[+CO_2]}$ sample fits, sediment and reference spectra were not well matched for second-neighbor backscattering (Fig. 5), indicating the lack of appropriate reference compounds. Individual shell fits of these spectra (not shown) suggest several Si/Al backscattering distances within the range expected for both feldspathoids and feldspars. Linear combination fits of $LOW_{[-CO_2]}$ sediments produced better results with the sodalite/cancrinite reference spectrum, consistent with Sr incorporation into the large cages of sodalite/cancrinite-type phases [23].

4. Discussion

We observed what would initially seem contradictory by measuring a decrease in CEC and SSA concurrent with an increase in clay sized particles along the sediment-waste reaction paths (Fig. 1, Table 1). However, these data sets are found to be internally consistent when the nature of precipitates formed as reaction products is considered. While sodalite and cancrinite fall into the same particle size range as 2:1 layer clay minerals, they are known to have SSA_{BET} and CEC_{Cohex} values that are an order of magnitude lower [23,42]. This lower CEC_{Cohex} is not a measure of actual feldspathoid structural charge because the large radius of the Cohex ion precludes its entry as a probe into many internal exchange sites [42]. Collectively, the effects of contaminant concentration and reaction time on SSA (lower SSA in HIGH and at 6 months) are consistent with an initial rapid dissolution of sediment clays followed by the gradual re-precipitation of neoprecipitates (also clay sized) and an overall higher dissolution rate in the LOW treatment. The diminished CEC post-reaction is consistent with the dissolution of surface-reactive particles.

4.1. Influence of contaminant concentration

Our results indicate that contaminant concentrations affect sediment geochemical reactions in STWL that ultimately control contaminant speciation and fate. This is despite the fact that contaminant species are trace components with orders-of-magnitude lower concentrations than major ions (Na^+, NO_3^-, $Al(OH)_4^-$, OH^-). Nonetheless, a contaminant concentration effect was observed in several independent characterization datasets. Quantitative-XRD performed on both the sediment bulk and fine fractions reveal that primary minerals quartz, illite, chlorite and plagioclase, as well as calcite in the [−CO_2] treatments, all undergo dissolution. Moreover XRD, FTIR, and TEM-EDS investigations indicate that nucleation and crystal growth of NO_3-feldspathoids occur in LOW treatments, but Ca–Sr rich chabazite-type zeolite forms in HIGH treatments. Deng et al. [22] reported that Cs concentration (from 10^{-4} to 0.5×10^{-1} M) affected the type of neoprecipitates in caustic solutions at short-term (<8 weeks), but hypothesized that this effect would not affect the formation of cancrinite/sodalite at concentrations relevant to the Hanford site. Chorover et al. [14] showed that initial Cs and Sr concentrations strongly affect the rate of neophase formation in STWL-kaolinite systems, with more rapid precipitation at lower Cs/Sr concentrations and the formation of Al-chabazite only at high concentration of Cs/Sr (10^{-3} M). This was attributed to inhibition of hydroxide-promoted kaolinite dissolution by adsorbed Sr.

Here we show for the first time that initial contaminant concentration also affects the trajectory of neophase precipitation in the multi-component Hanford sediments themselves at field-relevant conditions. TEM and XRD measurements indicate the neoprecipitates formed in sediments reacted at HIGH contaminant concentration are principally chabazite, whereas those formed at LOW contaminant concentrations are mostly feldspathoids that increase in abundance with reaction time. Characterization of Sr coordination in reacted FF sediments by EXAFS is consistent with this assessment. EXAFS data indicates Sr association mostly with a chabazite-type zeolite in HIGH (although some substitution of Sr for Ca in strätlingite cannot be ruled out), and with feldspathoid-type phases in LOW. Strontium coordination in chabazite is more readily detected by Sr-EXAFS because divalent cations tend to occupy a cation site in the large cage at the opening of the 6-ring of the D6R cage (cation site 1 of [43]). In this site, the cation is partially dehydrated and regularly coordinated to three framework O atoms and to five or six other O or H_2O molecules [35,43], which lowers the static disorder between the cation and the 6 second-neighbor Al/Si atoms. In contrast, Sr in sodalite/cancrinite phases can occupy cation sites in the large central cage where it partially dehydrates and bonds to framework O atoms. This results in variable site occupancies, higher static disorder, and lower average backscattering amplitude from framework Al/Si atoms [17,23].

In high pH, Na-bearing aluminosilicate solutions, it has been shown that the introduction of Ca^{2+} triggers the transformation

of sodalite into cancrinite [44]. In Hanford sediments, when high affinity Cs sites (micaceous FES) were exhausted, Cs was shown to partition into neophases [11,13]. Therefore the EDS-detected Cs in the feldspathoids is most likely behaving similar to Na in terms of its site occupancy. The structural preference for monovalent ions has been noted in similar systems where high concentrations of divalent cations trigger the formation of intermediate metastable phases that slow the formation of sodalite/cancrinite [22]. The stoichiometric ratio of monovalent to divalent cation concentration is known to control zeolite versus feldspathoid formation [45]. Thus we interpret the predominance of chabazite in the HIGH treatment to be a result of higher divalent (Sr) concentration initially in solution. The threshold divalent concentration required to shift the trajectory of neoprecipitate formation is low ([Sr] = 10^{-5} M) when compared with the high background concentrations of Na (2.0 M). This highlights a key observation of the current study: variation in concentrations of trace contaminant cations directs the trajectory of neoprecipitate formation and contaminant fate in these caustic systems.

4.2. Influence of pCO_2

As shown by XRD and EXAFS, pCO_2 also has a strong influence on mineral transformation and Sr speciation during sediment-STWL reaction. The effect hinges on formation or dissolution of CO_3-bearing minerals phases. During reaction with atmospheric pCO_2, native calcite persists, whereas when CO_2 is excluded, $CaCO_3$ dissolution occurs. Calcite dissolution affects aluminosilicate precipitation reactions directly because the Ca^{2+} released in the absence of CO_2 reacts with Al from STWL and Si from silicate mineral dissolution to form the calcium alumino-silicate hydrate, strätlingite ($Ca_2Al_2SiO_2(OH)_{10}{\cdot}3H_2O$). This phase is observed in the XRD data for all [$-CO_2$] treatments (Fig. 2, Table 4). The formation of strätlingite during hydration of high pH, Ca–Al–Si–H cement systems has been widely observed at room temperature [32,46–48] where the reaction:

$$Ca_2Al_2SiO_2(OH)_{10} \cdot 3H_2O(s) \Leftrightarrow 2Ca^{2+} + 2Al(OH)_4^- + Si(OH)_3^- + OH^- + 2H_2O$$

has a $\Delta G_r^\circ = -5709.63$ [kJ mol^{-1}] and a $\log K_{s0} = -20.49$ [49].

Natural strätlingite, analyzed by Rinaldi et al. [36], showed frequent substitutions of Ca by Sr in its octahedral (brucite-type) layer. Our results suggest that precipitation of strätlingite may hamper precipitation of feldspathoids in the HIGH$_{[-CO_2]}$ treatment (12 mo data, Table 4). Strätlingite formation consumes a higher molar ratio of soluble Al to Si and thereby diminishes solution phase supersaturation with respect to sodalite and cancrinite. Chabazite supersaturation is likely less affected because of its higher Si:Al ratio. Thus, in the HIGH treatments, it is likely that formation of feldspathoids and associated sequestration of Sr and Cs is indirectly controlled by native sediment calcite dissolution. Indeed, dissolution of native calcite ($CaCO_3$) is observed by quantitative XRD, and strontianite ($SrCO_3$) formation is observed in the EXAFS spectra in the [$+CO_2$] HIGH treatments only (Fig. 5 and Table 4).

5. Implications for Hanford site decontamination strategies

Understanding contaminant sequestration paths and processes is a first step toward site remediation and closure. Vadose zone infiltration of tank waste results in gradient-impacted plumes where spatially distributed contaminant concentrations, reaction times, and pCO_2 affect heterogeneity in contaminant fate. In this work, characterization and quantification of mineralogical transformations and associated contaminant sequestration provides insight needed for prediction of contaminant stability subsequent to source removal. For example, at atmospheric pCO_2, the precipitation of stable Sr and Cs containing feldspathoids occurs after 12 mo of reaction at high contaminant concentrations, whereas in absence of CO_2, chabazite remains dominant, resulting in effective contaminant Sr sequestration and – we predict based on prior work [13,14,16,17] – slower subsequent desorption. In samples with low contaminant concentration, formation of mixed sodalite and cancrinite leads to effective stabilization of contaminant Sr and to some extent, Cs [25]. In summary, both pCO_2 and contaminant concentration have strong effects on contaminant sequestration pathways and, therefore on product stability under any remediation scenario.

Acknowledgements

This research is funded by the Environmental Remediation Science Program (ERSP), Biological and Environmental Research (BER), Office of Science, U.S. Department of Energy, Grant no. DE-FG02-06ER64190. Dr. T. Fridriksson (ISOR, Iceland) kindly provided the reference chabazite sample. Portions of this research were carried out at the Stanford Synchrotron Radiation Lightsource, a national user facility operated by Stanford University on behalf of the U.S. Department of Energy, Office of Basic Energy Sciences. The SSRL Structural Molecular Biology Program is supported by the Department of Energy, Office of Biological and Environmental Research, and by the National Institutes of Health, National Center for Research Resources, Biomedical Technology Program.

Appendix A. Supplementary data

Supplementary data associated with this article can be found, in the online version, at doi:10.1016/j.jhazmat.2011.09.063.

References

[1] C.T. Johnston, S.F. Agnew, J.R. Schoonover, J.W. Kenney, B. Page, J. Osborn, R. Corbin, Raman study of aluminum speciation in simulated alkaline nuclear waste, Environ. Sci. Technol. 36 (2002) 2451–2458.
[2] F.M. Mann, K.C. Burgard, W.R. Root, R.J. Puigh, S.H. Finfrock, R. Khaleel, D.H. Bacon, E.J. Freeman, B.P. McGrail, S.K. Wurstner, P.E. LaMont, Hanford immobilized low-activity waste performance assessment, in: DOE/ORP-2000-24, Office of River Protection, Department of Energy, Richland, WA, USA, 2001.
[3] D.I. Kaplan, Geochemical data package for the Hanford immobilized low-activity tank waste performance assessment (ILAWPA), in: PNNL-11964, Pacific Northwest National Laboratory, Richland, WA, USA, 2000.
[4] C. Liu, J.M. Zachara, O. Qafoku, S.C. Smith, Effect of temperature on Cs^+ sorption and desorption in subsurface sediments at the Hanford site, USA, Environ. Sci. Technol. 37 (2003) 2640–2645.
[5] J.P. McKinley, C.J. Zeissler, J.M. Zachara, R.J. Serne, R.M. Lindstrom, H.T. Schaef, R.D. Orr, Distribution and retention of ^{137}Cs in sediments at the Hanford Site, Washington, Environ. Sci. Technol. 35 (2001) 3433–3441.
[6] J.M. Zachara, S.C. Smith, C. Liu, J.P. McKinley, R.J. Serne, P.L. Gassman, Sorption of Cs^+ to micaceous subsurface sediments from the Hanford site, USA, Geochim. Cosmochim. Acta 66 (2002) 193–211.
[7] J.M. Zachara, J. Serne, M. Freshley, F. Mann, F. Anderson, M. Wood, T. Jones, D. Myers, Geochemical processes controlling migration of tank wastes in Hanford's vadose zone, Vadose Zone J. 6 (2007) 985–1003.
[8] M. Denham, D. Kaplan, C. Yeager, Groundwater radioiodine: prevalence, biogeochemistry, and potential remedial approaches, in: SNRL-STI-2009-00463, Savannah River National Laboratory, Department of Energy, Aiken, SC, USA, 2009.
[9] R.E. Gephart, Hanford: A Conversation about Nuclear Waste and Cleanup, Battelle Press, Columbus, OH, 2003.
[10] B.R. Bickmore, K.L. Nagy, J.S. Young, J.W. Drexler, Nitrate-cancrinite precipitation on quartz sand in simulated Hanford tank solutions, Environ. Sci. Technol. 35 (2001) 4481–4486.
[11] J. Chorover, S. Choi, P. Rotenberg, R.J. Serne, N.A. Rivera, C. Strepka, A. Thompson, K.T. Mueller, P.A. O'Day, Silicon control of strontium and cesium partitioning in hydroxide-weathered sediments, Geochim. Cosmochim. Acta 72 (2008) 2024–2047.
[12] W. Um, R.J. Serne, S.B. Yabusaki, A.T. Owen, Enhanced radionuclide immobilization and flow path modifications by dissolution and secondary precipitates, J. Environ. Qual. 34 (2005) 1404–1414.
[13] S. Choi, M.K. Amistadi, J. Chorover, Clay mineral weathering and contaminant dynamics in a caustic aqueous system: I. Wet chemistry and aging effects, Geochim. Cosmochim. Acta 69 (2005) 4425–4436.

[14] J. Chorover, S. Choi, M.K. Amistadi, K.G. Karthikeyan, G. Crosson, K.T. Mueller, Linking cesium and strontium uptake to kaolinite weathering in simulated tank waste leachate, Environ. Sci. Technol. 37 (2003) 2200–2208.
[15] H. Zhao, Y. Deng, J.B. Harsh, M. Flury, J.S. Boyle, Alteration of kaolinite to cancrinite and sodalite by simulated Hanford tank waste and its impact on cesium retention, Clays Clay Miner. 52 (2004) 1–13.
[16] S. Choi, G. Crosson, K.T. Mueller, S. Seraphin, J. Chorover, Clay mineral weathering and contaminant dynamics in a caustic aqueous system: II. Mineral transformation and microscale partitioning, Geochim. Cosmochim. Acta 69 (2005) 4437–4451.
[17] S. Choi, P.A. O'Day, N.A. Rivera, K.T. Mueller, M.A. Vairavamurthy, S. Seraphin, J. Chorover, Strontium speciation during reaction of kaolinite with simulated tank-waste leachate: bulk and microfocused EXAFS analysis, Environ. Sci. Technol. 40 (2006) 2608–2614.
[18] G.S. Crosson, S.Y. Choi, J. Chorover, M.K. Amistadi, P.A. O'Day, K.T. Mueller, Solid-state NMR identification and quantification of newly formed aluminosilicate phases in weathered kaolinite systems, J. Phys. Chem. B 110 (2006) 723–732.
[19] K. Mashal, J.B. Harsh, M. Flury, A.R. Felmy, Analysis of precipitates from reactions of hyperalkaline solutions with soluble silica, Appl. Geochem. 20 (2005) 1357–1367.
[20] K. Mashal, J.B. Harsh, M. Flury, A.R. Felmy, H.T. Zhao, Colloid formation in Hanford sediments reacted with simulated tank/waste, Environ. Sci. Technol. 38 (2004) 5750–5756.
[21] N.P. Qafoku, C.C. Ainsworth, J.E. Szecsody, D.L. Bish, J.S. Young, D.E. McCready, O.S. Qafoku, Aluminum effect on dissolution and precipitation under hyperalkaline conditions: II. Solid phase transformations, J. Environ. Qual. 32 (2003) 2364–2372.
[22] Y.J. Deng, M. Flury, J.B. Harsh, A.R. Felmy, O. Qafoku, Cancrinite and sodalite formation in the presence of cesium, potassium, magnesium, calcium and strontium in Hanford tank waste simulants, Appl. Geochem. 21 (2006) 2049–2063.
[23] N. Rivera, S. Choi, C. Strepka, K. Mueller, N. Perdrial, J. Chorover, P.A. O'Day, Cesium and strontium incorporation into zeolite-type phases during homogeneous nucleation from caustic solutions, Am. Miner. (2011), doi:10.2138/am.2011.3789.
[24] C.I. Steefel, S. Carroll, P.H. Zhao, S. Roberts, Cesium migration in Hanford sediment: a multisite cation exchange model based on laboratory transport experiments, J. Contam. Hydrol. 67 (2003) 219–246.
[25] A. Thompson, C.I. Steefel, N. Perdrial, J. Chorover, Contaminant desorption during long-term leaching of hydroxide-weathered Hanford sediments, Environ. Sci. Technol. 44 (2010) 1992–1997.
[26] W. Um, R.J. Serne, K.M. Krupka, Linearity and reversibility of iodide adsorption on sediments from Hanford, Washington under water saturated conditions, Water Res. 38 (2004) 2009–2016.
[27] W. Um, R.J. Serne, Sorption and transport behavior of radionuclides in the proposed low-level radioactive waste disposal facility at the Hanford site, Washington, Radiochim. Acta 93 (2005) 57–63.
[28] R.G. Riley, J.M. Zachara, Chemical Contaminants on DOE Lands and Selection of Contaminant Mixtures for Subsurfaces Sciences Research, U.S. Department of Energy, Office of Energy Research, Washington, DC, USA, 1992.
[29] L.R. Hossner, Dissolution for total elemental analysis, in: D.L. Sparks (Ed.), Methods of Soil Analysis: Part 3—Chemical Methods, Soil Science Society of America, Madison, WI, 1996, pp. 49–64.
[30] H. Ciesielski, T. Sterckeman, Determination of cation exchange capacity and exchangeable cations in soils by means of cobalt hexamine trichloride. Effects of experimental conditions, Agronomie 17 (1997) 1–7.
[31] J. Lande, S. Webb, A. Mehta, Area Diffraction Machine Software, 2007–2010.
[32] J. Ding, Y. Fu, J.J. Beaudoin, Strätlingite formation in high-alumina cement – silica fume systems – significance of sodium-ions, Cem. Concr. Res. 25 (1995) 1311–1319.
[33] J.C. Buhl, J. Löns, Synthesis and crystal structure of nitrate enclathrated sodalite $Na_8[AlSiO4]_6(NO_3)_2$, J. Alloys Compd. 235 (1996) 41–47.
[34] J.C. Buhl, F. Stief, M. Fechtelkord, T.M. Gesing, U. Taphorn, C. Taake, Synthesis, X-ray diffraction and MAS NMR characteristics of nitrate cancrinite Na-7.6$[AlSiO_4]$(6)(NO_3)(1.6)(H_2O)(2), J. Alloys Compd. 305 (2000) 93–102.
[35] A. Alberti, E. Galli, G. Vezzalini, E. Passaglia, P.F. Zanazzi, Position of cations and water-molecules in hydrated chabazite—natural and Na-exchanged, Ca-exchanged, Sr-exchanged and K-exchanged Chabazites, Zeolites 2 (1982) 303–309.
[36] R. Rinaldi, M. Sacerdoti, E. Passaglia, Strätlingite—crystal-structure, chemistry, and a reexamination of its polytype vertumnite, Eur. J. Miner. 2 (1990) 841–849.
[37] W.B. White, The carbonate minerals, in: V.C. Farmer (Ed.), The Infrared Spectra of Minerals, Mineralogical Society, London, 1974, pp. 227–284.
[38] O.S. Pokrovsky, J.A. Mielczarski, O. Barres, J. Schott, Surface speciation models of calcite and dolomite/aqueous solution interfaces and their spectroscopic evaluation, Langmuir 16 (2000) 2677–2688.
[39] G. Della Ventura, G.D. Gatta, G.J. Redhammer, F. Bellatreccia, A. Loose, G.C. Parodi, Single-crystal polarized FTIR spectroscopy and neutron diffraction refinement of cancrinite, Phys. Chem. Miner. 36 (2009) 193–206.
[40] J.M. Alia, Y.D. de Mera, H.G.M. Edwards, P.G. Martin, S.L. Andres, FT-Raman and infrared spectroscopic study of aragonite–strontianite ($CaxSr_1-xCO_3$) solid solution, Spectrochim. Acta Part A 53 (1997) 2347–2362.
[41] P. Benna, E. Bruno, Single-crystal in situ high-temperature structural investigation of the I(1)over-bar-I2/c phase transition in $Ca_{0.2}Sr_{0.8}Al_2Si_2O_8$ feldspar, Am. Miner. 88 (2003) 1532–1541.
[42] A. Derkowski, W. Franus, E. Beran, A. Czimerova, Properties and potential applications of zeolitic materials produced from fly ash using simple method of synthesis, Powder Technol. 166 (2006) 47–54.
[43] M. Calligaris, G. Nardin, L. Randaccio, P.C. Chiaramonti, Cation-site location in a natural chabazite, Acta Crystallogr. B 38 (1982) 602–605.
[44] B. Xu, P. Smith, C. Wingate, L. De Silva, The effect of calcium and temperature on the transformation of sodalite to cancrinite in Bayer digestion, Hydrometallurgy 105 (2010) 75–81.
[45] S.J. Chipera, J.A. Apps, Geochemical stability of natural zeolites, in: D.L. Bish, D.W. Ming (Eds.), Natural Zeolites: Occurrence, Properties, Applications, Reviews in Mineralogy & Geochemistry, 45, 2001, pp. 117–161.
[46] S. Kwan, J. Larosa, M.W. Grutzeck, Si-29 and Al-27 MAS NMR study of stratlingite, J. Am. Ceram. Soc. 78 (1995) 1921–1926.
[47] H.G. Midgley, P.B. Bhaskara Rao, Formation of stratlingite, $2CaO{\cdot}SiO_2{\cdot}Al_2O_3{\cdot}8H_2O$, in relation to hydration of high alumina cement, Cem. Concr. Res. 8 (1978) 169–172.
[48] N. Saikia, S. Kato, T. Kojima, Thermogravimetric investigation on the chloride binding behaviour of MK-lime paste, Thermochim. Acta 444 (2006) 16–25.
[49] B. Lothenbach, F. Winnefeld, Thermodynamic modelling of the hydration of Portland cement, Cem. Concr. Res. 36 (2006) 209–226.